Colorado Student Space Weather Experiment: Differential Flux Measurements of Energetic Particles in a Highly Inclined Low Earth Orbit

X. Li,[1,2] S. Palo,[2] R. Kohnert,[1] D. Gerhardt,[2] L. Blum,[1,2] Q. Schiller,[1,2] D. Turner,[3] W. Tu,[4] N. Sheiko,[1] and C. Shearer Cooper[1,2]

The Colorado Student Space Weather Experiment (CSSWE) is a three-unit (10 cm × 10 cm × 30 cm) CubeSat mission funded by the National Science Foundation; it was launched into a low Earth, polar orbit on 13 September 2012 as a secondary payload under NASA's Educational Launch of Nanosatellites program. The science objectives of CSSWE are to investigate the relationship of the location, magnitude, and frequency of solar flares to the timing, duration, and energy spectrum of solar energetic particles reaching Earth and to determine the precipitation loss and the evolution of the energy spectrum of radiation belt electrons. CSSWE contains a single science payload, the Relativistic Electron and Proton Telescope integrated little experiment (REPTile), which is a miniaturization of the Relativistic Electron and Proton Telescope (REPT) built at the Laboratory for Atmospheric and Space Physics. The REPT instrument will fly onboard the NASA Radiation Belt Storm Probes mission, which consists of two identical spacecraft launched on 30 August 2012 that will go through the heart of the radiation belts in a low-inclination orbit. CSSWE's REPTile is designed to measure the directional differential flux of protons ranging from 10 to 40 MeV and electrons from 0.5 to >3 MeV. Such differential flux measurements have significant science value, and a number of engineering challenges were overcome to enable these clean measurements to be made under the mass and power limits of a CubeSat. The CSSWE is an ideal class project, providing training for the next generation of engineers and scientists over the full life cycle of a satellite project.

1. INTRODUCTION

A full understanding of energetic particle dynamics in the near-Earth space environment is of scientific significance as well as of practical importance. Particularly at higher-latitude regions, energetic particles from the interplanetary medium, such as solar energetic particles (SEPs), have direct access to the Earth. Additionally, existing energetic particles in the magnetosphere, such as relativistic electrons in the outer radiation belt, can reach low altitudes following the magnetic field lines whose foot points map to high latitudes (>40°). This high-latitude, low-altitude region is also populated with many satellites as well as the international space station, from which various extravehicle activities have been performed. Energetic particles with energies of MeV can have

[1]Laboratory for Atmospheric and Space Physics, University of Colorado, Boulder, Colorado, USA.

[2]Department of Aerospace Engineering Sciences, University of Colorado, Boulder, Colorado, USA.

[3]Department of Earth and Space Sciences, University of California, Los Angeles, California, USA.

[4]Los Alamos National Laboratory, Los Alamos, New Mexico, USA.

Dynamics of the Earth's Radiation Belts and Inner Magnetosphere
Geophysical Monograph Series 199
© 2012. American Geophysical Union. All Rights Reserved.
10.1029/2012GM001313

harmful radiation effects on the bodies of astronauts and various deleterious effects on satellite subsystems through either single event upset or deep dielectric discharging [*Baker*, 2001, 2002]. Better measurement and understanding of the energetic particles in a highly inclined low Earth orbit (LEO) are the science objectives of the Colorado Student Space Weather Experiment (CSSWE) mission. CSSWE has also provided a unique opportunity for students to acquire hands-on experience, under the tutelage of experienced scientists and engineers, throughout the entire engineering process, gaining experience in data analysis and modeling, and gaining scientific insight on solar activity and its effects on the near-Earth space environment.

We will first discuss the science background and motivation for this project, the science measurement requirement, and expected science results and impact, before we provide the system description of the mission, followed by planned data analysis and interpretation, and modeling efforts and then discussion and summary.

1.1. Science Background and Motivation

Humankind has long been fascinated with the Sun and its relationship to our planet. *Sabine* [1852] was first to note that geomagnetic activity tracks the 11 year solar activity cycle. The first solar flare ever observed, in white light, was followed about 18 h later by a very large geomagnetic storm [*Carrington*, 1860]. The existence of the Earth's radiation belts was established in 1958 by James Van Allen and coworkers using simple Geiger counters on board Explorer-1 and -3 spacecraft. Since then, more advanced space missions have provided insight into the phenomenology and range of processes active on the Sun and in the radiation belts.

We now understand that coronal mass ejections (CMEs), which are episodic ejections of material from the solar atmosphere into the solar wind, are the link between solar activity and large, nonrecurrent geomagnetic storms, during which the trapped radiation belt electrons have their largest variations. There is a strong correlation between CMEs and solar flares, but the correlation does not appear to be a causal one. Rather, solar flares and CMEs appear to be separate phenomena, both resulting from relatively rapid changes in the magnetic structure of the solar atmosphere [e.g., *Gosling*, 1993].

1.1.1. Solar flares and solar energetic particles. Solar flares are very violent processes in the solar atmosphere that are associated with large-energy releases ranging from 10^{22} J for subflares, to more than 10^{32} J for the largest flares [*Priest*, 1981]. The strongest supported explanation for the onset of the impulsive phase of a solar flare is that it is due to magnetic reconnection of existing or recently emerged magnetic flux loops [*Aschwanden*, 2004, and references therein]. Magnetic reconnection accelerates particles, producing proton and electron beams that travel along flaring coronal loops. Some of the high-energy particles escape from the Sun and can reach the Earth's low-altitude, high-latitude regions.

Statistically, both the probability of observing energetic solar protons near the Earth as well as the maximum flux values observed are strongly dependent on the size of the flare and its position on the Sun. It is also now clear that the most intense and longest-lasting SEP events are produced by strong shocks in the solar wind driven by the fast CMEs [e.g., *Reames*, 1997]. It is currently believed that SEPs observed near Earth are of two basic populations. Events in one population, the so-called "impulsive" events, originate in flaring regions and typically last for several hours and have limited spatial extents (<30° in latitude and longitude) in the solar wind. In contrast, events in the other population, the so-called "gradual" events, tend to be more intense than the impulsive events, typically last for days, often spread over more than 180° in latitude and longitude and are strongly associated with CME-driven shock disturbances. In practice, since flares and CMEs often occur in conjunction with one another, many SEP events appear as hybrids of these two basic populations.

Crucial questions remain about exactly how and where both of the above populations are produced. In the case of flare events, a major uncertainty is how a given flare site connects magnetically to the interplanetary medium, i.e., the accessibility to, and extent of, open magnetic field lines in the vicinity of a flare site [*Cane and Lario*, 2006].

The time-intensity profiles of the SEP events observed in the ecliptic plane at 1 AU are organized in terms of the longitude of the observer with respect to the traveling CME-driven shock [*Cane et al.*, 1988; *Kanekal et al.*, 2008]. SEP events generated from the western longitudes have rapid rises followed by gradual decreasing intensities, while SEP events generated from eastern longitudes show slowly rising intensity enhancement structured around the arrival of the CME-driven shocks. It is clear that the location of the event is very important regarding how these SEPs affect the Earth's environment. This longitudinal dependence of the time-intensity profiles, together with the rate at which the particle intensities increase or decrease, have been used to predict the arrival of CME-driven shocks at 1 AU [*Smith et al.*, 2004; *Vandegriff et al.*, 2005].

1.1.2. Earth's radiation belts. Earth's radiation belts are usually divided into the inner belt, centered near 1.5 Earth radii (R_E) from the center of the Earth when measured in the

equatorial plane, and the outer radiation belt that is most intense between 4 and 5 R_E. These belts form a torus around the Earth, and many important satellite orbits go through them, including GPS satellites, spacecraft at geosynchronous orbit (GEO), and those in highly inclined LEO.

The Earth's outer radiation belt consists of electrons in the energy range from keV to MeV. Compared to the inner radiation belt, which usually contains somewhat less energetic electrons but an extremely intense population of protons extending in energy up to several hundreds of MeV or even GeV, the outer belt consists of energetic electrons that show a great deal of variability that is well correlated with geomagnetic storms and high speed solar wind streams [*Williams*, 1966; *Paulikas and Blake*, 1979; *Baker et al.*, 1979]. Figure 1 shows measurements of radiation belt electrons and protons by the Solar, Anomalous, and Magnetospheric Particle Explorer (SAMPEX), ~550 km altitude and 82° inclination, from launch to the end of 2009 together with the sunspot number and the *Dst* index, which indicates the onset, duration, and magnitude of magnetic storms. The outer belt exhibits a strong seasonal and solar cycle variation. It was most intense, on average, during the descending phase of the sunspot cycle (1993–1995; 2003–2005), weakest during sunspot minimum (1996–1997; 2007–2009), and then became more intense again during the ascending phase of the solar cycle (1997–1999). Seasonally, the outer belt is most intense around the equinoxes [*Baker et al.*, 1999] and also penetrates the deepest around the equinoxes [*Li et al.*, 2001]. In Figure 1, the vertical yellow bars along the horizontal axis mark equinoxes. Another remarkable feature of Figure 1 is the correlation of the inward extent of MeV electrons with the *Dst* index, which is also referred to as the magnetic storm index.

1.2. Science Measurement Requirements

CSSWE is a three-unit (10 cm × 10 cm × 30 cm) CubeSat mission. Resources are limited. Any design is subject to the constraints of mass, power, data rate, and budget. To reach the science objectives described earlier and take into consideration various limitations of a CubeSat and what existing measurements are already available, the following science measurement requirements are established: (1) electron differential flux measurements between 0.5 and 3 MeV, and integral flux measurements for >3 MeV, (2) proton differential flux measurements between 10 and 40 MeV, (3) time cadence: 6 s.

Even the above general requirements were not settled until various design work and trade studies were performed. The

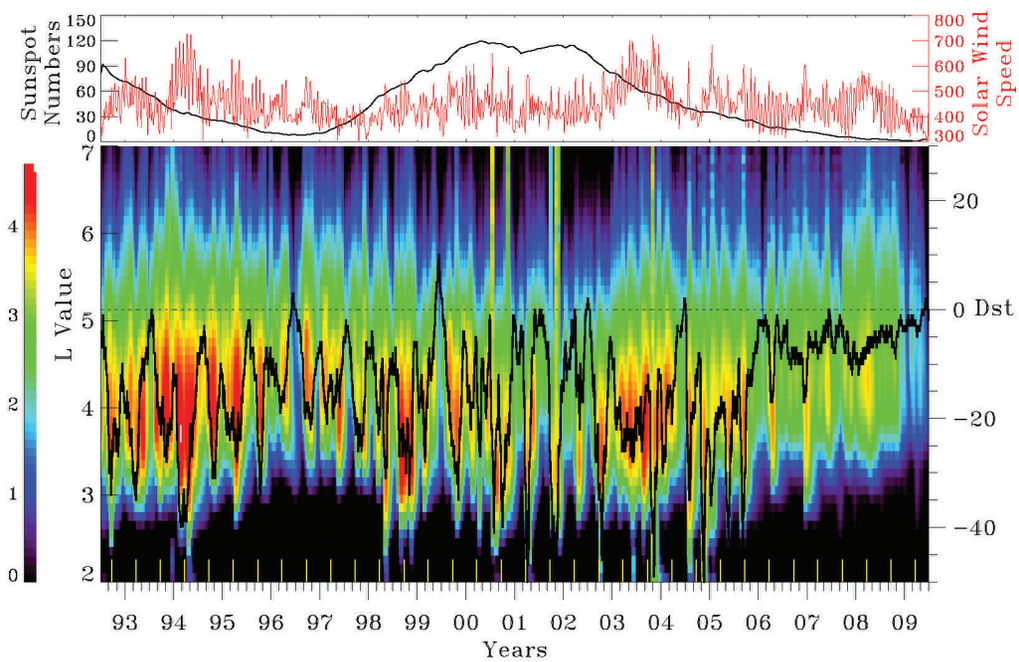

Figure 1. (top) Variations of yearly window-averaged sunspot numbers (black curve) and weekly window averaged solar wind speed (km s^{-1}, red curve). (bottom) Monthly window-averaged, color-coded in logarithm, and sorted in L (L bin: 0.1) electron fluxes of 2–6 MeV (# cm^{-2} s^{-1} sr^{-1}) by SAMPEX since its launch (3 July 1992) into a low-altitude (550 km × 600 km) and highly inclined (82°) orbit. The superimposed black curve represents monthly averaged *Dst* index. From *Li et al.* [2011].

time cadence is strictly limited by the downlink rate available based on one ground station built for this mission. The particle energy range is limited by the speed of electronic resolution and the available shielding mass, which is associated with the S/N ratio. Detailed spacecraft and instrument design will be described later.

1.3. Expected Science Results and Impact

1.3.1. Solar energetic particles. There are no existing differential flux measurements for protons in the tens of MeV range in LEO. NOAA/NPOES in LEO provide integral measurement of protons between 100 keV to low MeV. GOES at GEO have both integral and differential measurements of protons between 1 and 100 MeV. Relativistic Electron and Proton Telescope integrated little experiment (REPTile) on CSSWE will provide measurements of the differential flux of protons at LEO, which are critical for investigating the geomagnetic cutoff variations during SEP events and their implication for the radiation environment at the International Space Station [*Leske et al.*, 2001]. However, any significant science results have to be achieved with coordination with other available measurements and modeling efforts. For example, to study how the flare location, magnitude, and frequency relate to the timing, duration, and energy spectrum of SEPs reaching Earth, the information about the solar flare intensity and location, which are provided by other missions, namely, NASA Solar Dynamic Observatory (SDO) and/or NOAA GOES are required.

1.3.2. Outer radiation belt electrons. Instruments onboard SAMPEX, though a wonderful mission for its original objectives, were not designed to make accurate measurements of the outer radiation belt electrons. For example, they lack differential flux measurements for MeV electrons. With REPTile on CSSWE, we will have measurements necessary to better determine the electron energy spectrum. These measurements will help us to better understand the acceleration mechanisms and loss processes of the outer radiation belt electrons.

Measurements of outer belt electrons made by REPTile will also be useful for comparisons with those made by NASA's Radiation Belt Storm Probes (RBSP) mission. The RBSP satellites will travel through the heart of the outer belt, where they will make important measurements of outer belt fluxes and the various types of plasma waves that are important in electron acceleration and loss. However, for electrons and protons to precipitate into the atmosphere (a major loss mechanism), their equivalent equatorial pitch angle (PA) has to be very small, 2°–5° depending on their actual locations. The instruments onboard RBSP, sophisticated as they are, cannot resolve the loss cone distribution because they stay close to the equator. Thus, it will be difficult to determine the precipitation loss from their measurements. Though REPTile measures a mixed population of precipitating as well as trapped radiation belt electrons and protons from its low-altitude high-inclination orbit, combining REPTile measurements at LEO with modeling efforts (to be discussed in detail later) will enable us to determine the precipitation loss. By comparing flux measurements made by RBSP and REPTile, better estimates can be made of the trapped electron population and the precipitating population.

1.3.2.1. Acceleration mechanisms. How the outer radiation belt is formed in the Earth's magnetosphere remains one of the most intriguing puzzles in space physics. For some time, it was thought to be well understood at least in its general outlines. However, recently, the paradigm for explaining the creation of the outer belt electrons has been shifting from one using almost exclusively the theory of radial diffusion to one emphasizing more the role of waves [*Li et al.*, 1999; *Horne et al.*, 2005; *Shprits et al.*, 2007; *Chen et al.*, 2007; *Bortnik and Thorne*, 2007; *Li et al.*, 2007; *Tu et al.*, 2009; *Turner et al.*, 2010], presumably chorus whistler waves, in local heating of radiation belt electrons. A key proof of this new paradigm is to see how the energy spectrum of the radiation belt electrons evolves. A hardening spectrum (higher-energy electrons increasing faster than lower-energy electrons) at a given location would support the theory of in situ heating of the electrons by waves. Because of its low-altitude orbit, CSSWE will measure outer belt electrons four times in one orbital period, ~1.5 h, or about 60 times in a day. With its differential flux measurements, REPTile will be able to provide the critical information of the evolution of the electrons' energy spectrum.

1.3.2.2. Loss mechanisms. Some waves, like electromagnetic ion cyclotron waves, can cause PA diffusion of electrons, sending some electrons into the loss cone. Other waves, like whistler mode chorus waves, can cause energy diffusion as well as PA diffusion. An important consequence of the PA variation is precipitation loss. REPTile measurements can help to determine how many of the outer radiation belt electrons are lost to the atmosphere. Also, when RBSP and CSSWE are at similar magnetic longitudes and L shells, comparative studies can be conducted in which waves and fluxes measured by RBSP near the equator and the heart of the belt are compared to the REPTile measurements in LEO to directly compare waves with electron loss.

In summary, the science impacts of CSSWE are to provide needed measurements of energetic protons and electrons at LEO, in combination with other available measurements, to

better address the following science questions: (1) How do solar flare location, magnitude, and frequency relate to the timing, duration, and energy spectrum of SEPs reaching Earth? (2) How do the loss rate and energy spectrum of the Earth's radiation belt electrons evolve?

2. SYSTEM DESCRIPTION OF THE CSSWE MISSION

2.1. Overview

CSSWE, like most satellites, is a collection of subsystems. In order to organize the subsystems, the requirements' flow down was defined throughout the mission development, bolstered by mass, power, data, and link budgets, as well as a risk analysis. A 3 U CubeSat is defined as a small volume (10 cm × 10 cm × 30 cm), small mass (< 4 kg), and completely autonomous (i.e., power, communications) satellite. Despite these strict requirements, CSSWE was delivered with margin in all budgets. The CSSWE architecture reflects the "keep it simple" method of satellite development; the system design was always simplified to meet requirements rather than designed to "push the envelope." Only two microcontrollers (MCUs) are present in the system, and two subsystems (attitude control system and thermal) are almost entirely passive. The command and data handling (C&DH) board and communication (COMM) radio were commercial off-the-shelf (COTS) purchases in an effort to minimize risk. Figure 2 shows the system block diagram of CSSWE. In the following sections, we will provide a general description of individual subsystems, with some more detailed description on the science payload, REPTile.

2.2. Structure and Thermal Design

The structural design of the CSSWE CubeSat began with the commercially available Pumpkin, Inc. 3 U aluminum chassis. The left image in Figure 3 shows a rendering of the aluminum shell of the CubeSat with custom-designed solar panels. The right side of Figure 3 shows the interior components of the CubeSat with the REPTile scientific instrument at the center and electronic boards (light blue) and battery (yellow) on the top of REPTile. The interior view shows the custom structural supports made to accommodate the relatively heavy instrument as well as all electrical components. The design of the interior structure was also driven by the CubeSat requirement that the satellite center of mass be within 2 cm of the geometric center, as well as the need for simple assembly and disassembly during integration and testing. All of the interior components assemble in a vertical stack, allowing the exterior shell to slide over the entire assembly during integration. Extensive finite element analysis was performed on the structural components to ensure that the CubeSat could survive a vibration environment three

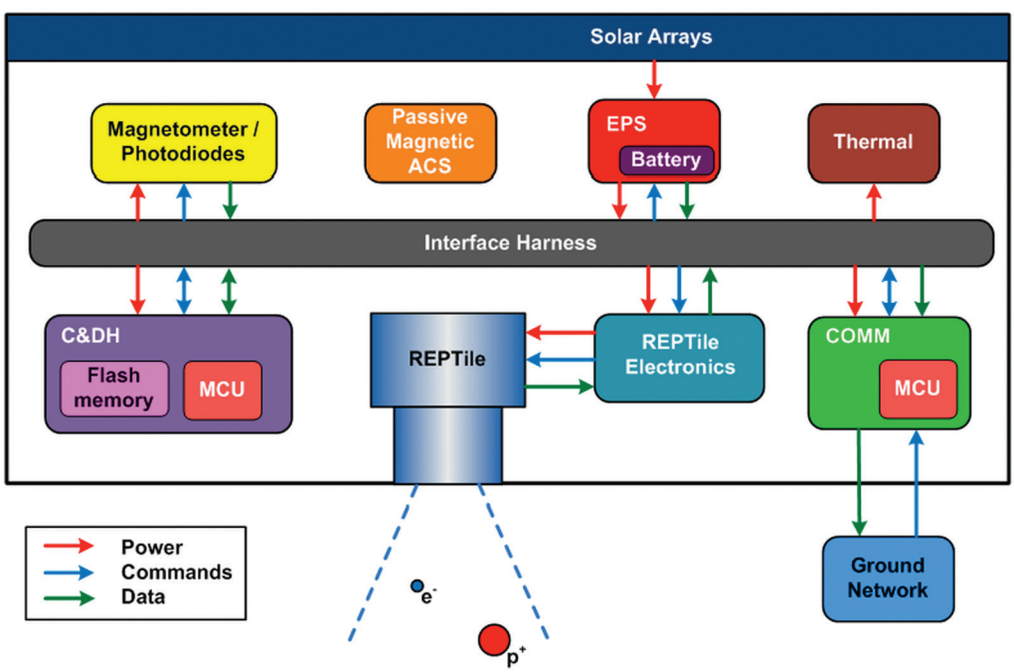

Figure 2. System block diagram of Colorado Student Space Weather Experiment (CSSWE), where e^- and p^+ represent energetic electrons and protons to be measured.

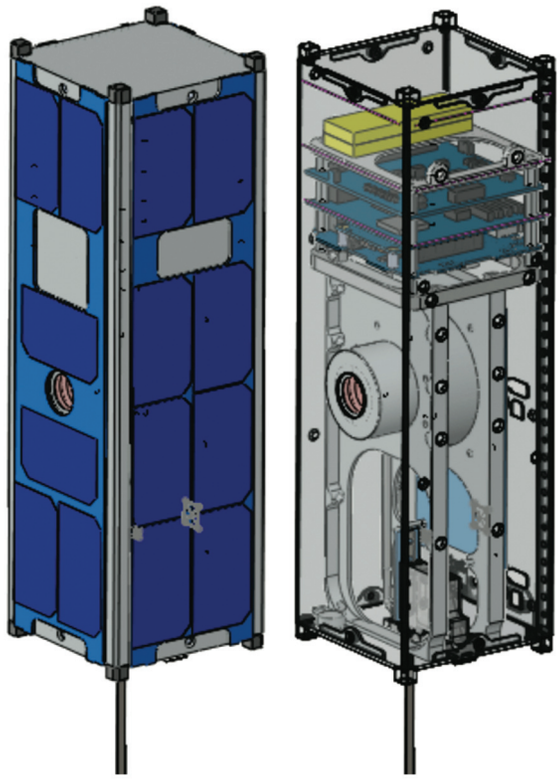

Figure 3. Three-dimensional rendering of the CSSWE CubeSat, (left) exterior view and (right) interior view.

sigma higher than expected during launch. Prelaunch qualification and acceptance random vibration testing confirmed that the structure met all strength requirements.

Figure 4 shows the completed flight model after final integration. The cutouts (e.g., the silver area between the solar cells in Figure 4) are radiative windows designed to keep the satellite electronics stack cool. The small slits visible in the top thermal window are two of four electronic ports used for preflight communication and battery charging. Detailed thermal analysis was performed on the entire system using Thermal Desktop, a software tool used to model thermal environments. Individual electronic boards were thermally modeled to provide a predicted on-orbit temperature profile for sensitive electronics. The radiative windows mentioned above were subsequently added to help radiate excess heat from the system, to maintain internal board temperatures within range of manufacturer specifications for all electronics components (between −30°C to +45°C).

2.3. Electric and Power System and Solar Arrays

CSSWE employs a direct energy transfer system that was designed, fabricated, and tested by the University of Colorado students. The CSSWE power system architecture was modeled after the design used for the University of Michigan's RAX mission [*Cutler et al.*, 2010].

Four independent solar array strings, one on each long-axis side of the CubeSat, are each fed into 8.8 V regulators with isolation diodes on the output. Solar arrays, designed and fabricated by the University of Colorado students, employ 28% efficient, uncovered, triple junction solar cells. The 6–8.4 V bus is driven by the voltage of the 8.4 V lithium polymer battery. The 3.3 and 5 V regulated buses are powered from the battery bus and supply power to most of the subsystem electronics. The exceptions to this are the antenna deployment module and the transmitter power amplifier, which are powered directly from the 6–8.4 V power bus. An external charge port allows the spacecraft to be powered by an external power supply for ground test and mission simulations in the laboratory. The battery can be disconnected from the bus by either of two series switches, the Remove Before Flight (RBF) switch or the deployment switch, as is required in the CalPoly CubeSat Design Specification. The RBF switch is used while testing in the laboratory and is closed upon final integration into the P-POD launcher. The deployment switch remains open, while the spacecraft is integrated in the P-POD launcher. The deployment switch closes upon spacecraft deployment, connecting the battery to the bus and turning the spacecraft on once on orbit. Figure 5 shows the schematics of the electrical and power system, with solar cell inputs (PVX and PVY) on the left; 3.3, 5, and 6–8.4 V outputs to various other subsystems are shown on the right.

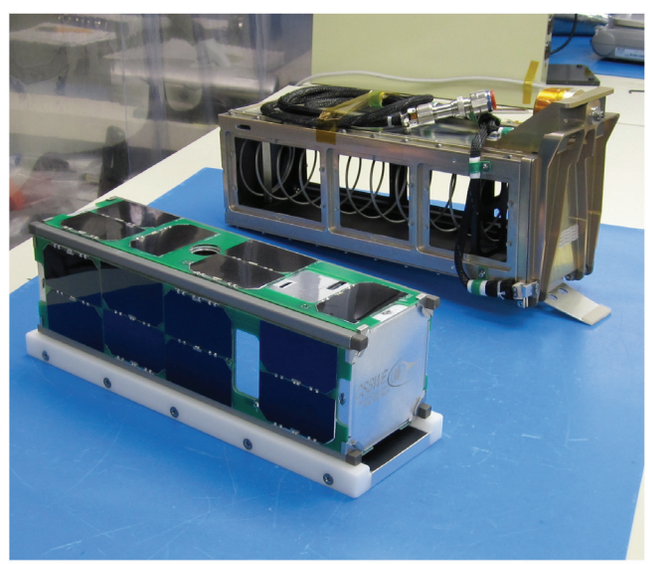

Figure 4. Final flight model and P-POD launcher.

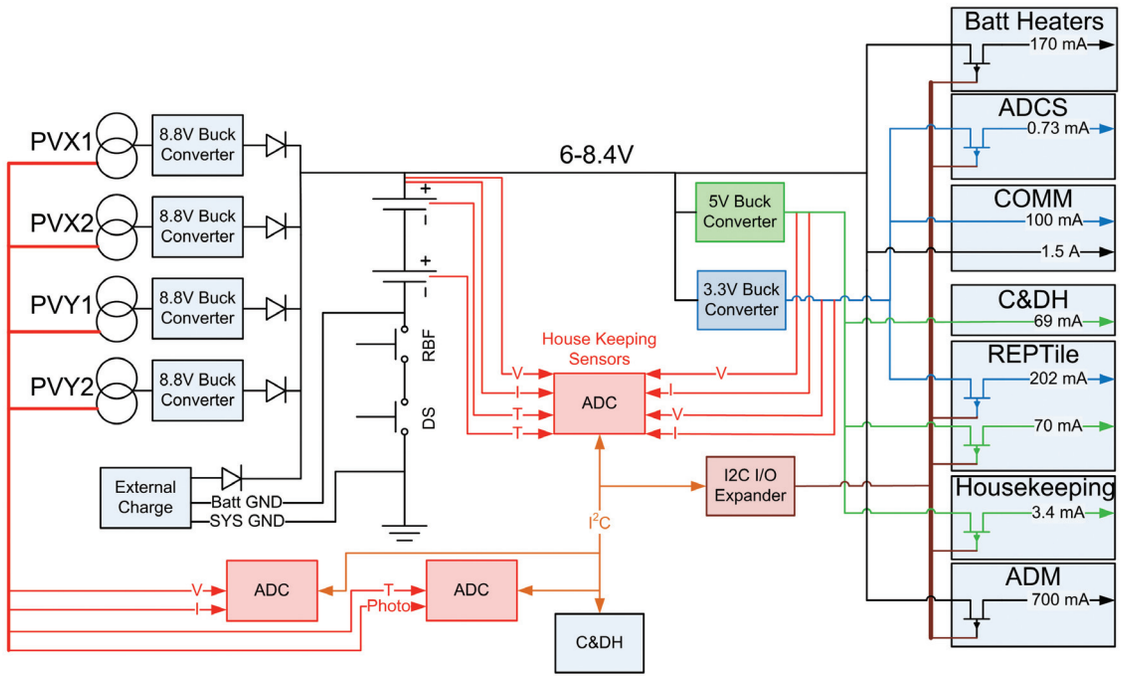

Figure 5. Electrical and power system electric diagram.

2.4. Command and Data Handling System

The C&DH system for the CSSWE CubeSat utilizes an off-the-shelf processor module from Pumpkin, Inc. that uses a 16 bit MCU, the MSP430 from Texas Instruments. The MCU runs at 8 MHz and has 8 kb of random-access memory; this allows CSSWE to meet mission requirements while providing ultralow power consumption to reduce load on the battery. The C&DH firmware was written in C, and run under the Salvo real-time operating system. It was developed using CrossStudio for MSP430 from Rowley Associates Ltd. The processor module involves additional hardware including an interface to a secure digital (SD) card that is used to store science and housekeeping data, log files, and configuration parameters.

C&DH communicates with nearly every other subsystem in the satellite; most interfaces use the Inter-Integrated Circuit protocol, an interface often used for data acquisition. The only exceptions are communication with the hardware supporting the SD card, which uses Serial Peripheral Interface, and communication with the radio, which uses asynchronous serial. The interface to the radio and SD card was dictated by the hardware manufacturers.

The C&DH firmware has five main tasks: (1) responding to commands from the ground, (2) acquiring and storing science data, (3) acquiring and storing housekeeping data, (4) deploying the antenna, and (5) controlling the battery heaters. This simplicity is, in part, due to the overall design goal of minimal autonomy: to build the system in a way that reduces the number of decisions that C&DH makes on its own, while ensuring that enough information is available to operators on the ground to make informed decisions. C&DH is required to make a few autonomous choices; two of them have been mentioned already: deploying the antenna and controlling the battery heaters (to maintain the battery within operational temperature bounds even when out of range of the ground station). In addition, C&DH automatically drops into safe mode (and stops science operations) if it determines that the state of charge of the battery has fallen to a critically low level. Both the temperature settings of the battery heaters and the determination of whether the battery is "critically low" are controlled by parameters uploaded from the ground, allowing controllers to modify the spacecraft's operation in case of sensor malfunction on orbit. Additionally, CSSWE uses two independent watchdogs to ensure that neither the communications system (COMM) nor C&DH "locks up." If either subsystem does not respond to its associated watchdog, a soft reset is performed.

The storing of data onto the SD card takes place in two distinct streams. First of all, science data from the REPTile instrument and attitude data from the magnetometer are acquired and stored every 6 s. Second, housekeeping data (including voltages, currents, and temperatures from various locations on the spacecraft) are acquired every minute, and

then every 10 min the minimum, maximum, and average values are stored to the SD card. Both streams of data are stored in time-offset files that allow C&DH to easily respond to ground requests for data from particular time ranges.

Commands exist to allow the ground to start and stop science mode, request transmission of specific subsets of the acquired data, update parameters controlling system operation, request transmission of housekeeping sensor values, and perform diagnostic functions. Communication packets are password protected to prevent unauthorized users from commanding the spacecraft.

2.5. Communications System

The CSSWE team chose a half-duplex communications architecture operating in the 70 cm band, primarily to reduce the complexity of the system. Given the size of the data product and the minimal amount of commanding required for CSSWE, sharing the uplink and downlink does not have a significant negative impact on our link budget.

The communications system onboard the spacecraft utilizes the AstroDev Lithium (Li-1) radio, which operates over a wide range of frequencies and temperatures, is 40% power efficient, and can output 34 dBm of RF power. Additionally, the Li-1 radio supports the AX.25 packet radio protocol at a rate of 9.6 kbit s^{-1} across the RF link and up to 115.2 kbit s^{-1} between the radio and C&DH over the serial link. Assuming 21.75 min of communications time per day, calculated using the Satellite Took Kit for our nominal orbit and a ground station in Boulder, we have the capacity to downlink 1.195 MB d^{-1}, providing almost 50% more link capacity than is required for the mission.

A monopole was selected for the satellite antenna configuration after testing numerous options. The total length of the deployed antenna is 48.3 cm. The matching and tuning of the antenna provided excellent performance over our operating frequency with a maximum antenna gain in excess of 2 dBi for a reasonably omnidirectional antenna. Figure 6 shows the measured gain pattern of the CSSWE COMM system before and after antenna deployment. The deployed gain drops below −5 dBi only in the regions along the axis of the antenna, as well as at the small nulls near ±125° from the exposed end of the antenna. The results of orbit simulations indicate that CSSWE is rarely in an attitude and at a range where the link cannot be closed through this null in the pattern. Given our testing and analysis, we are confident that the communications system will operate as designed and will meet all the mission requirements for commanding and data throughput.

2.6. Ground Network

To operate the CSSWE CubeSat, a ground station has been built on the rooftop of the Laboratory for Atmospheric and

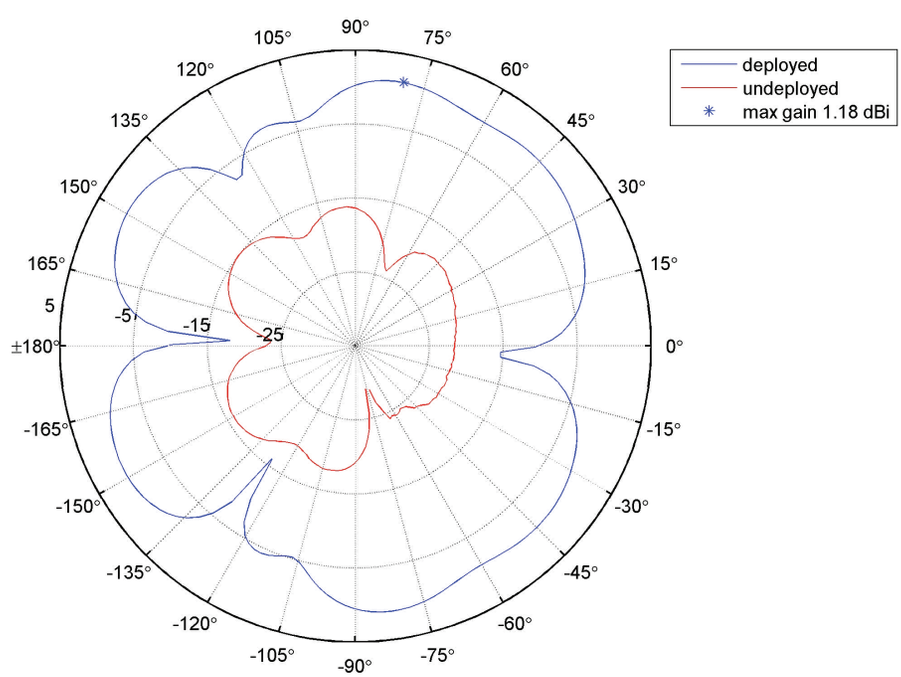

Figure 6. Antenna gain patterns before and after antenna deployment, as measured through anechoic chamber testing.

Space Physics (LASP). The CSSWE ground station operates in half-duplex mode, communicating at 437.345 MHz (UHF) for the uplink and downlink, the frequency designated to us by the International Amateur Radio Union. Commands are packetized and sent through Instrument and Spacecraft Interface Software (ISIS), commanding software that was inherited by LASP from the NOAA GOES-R program and has been customized for our uses. The Kantronics KAM XL terminal node controller modulates/demodulates the signal, and the Kenwood TS-2000 radio is used to communicate at the UHF band. Two M2 436CP42 cross Yagi antennas will be used, each with a gain of ~17 dBdc and a circular beamwidth of 21°. The antennas are pointed using a Yaesu G5500 azimuth-elevation rotator controlled by SatPC32, a software package developed for use with amateur satellites. This program also controls RF to account for Doppler shift during passes. The antennas and rotator are mounted on an 8 foot tower installed on the LASP roof and connected to the ground station control room with over ~200 feet of low-loss cabling, adding a total of −5.4 dBm loss to the RF signal. A block diagram of the ground station command and control chains is illustrated in Figure 7. The ground station has been fully tested and was used to command the satellite in a simulated on-orbit scenario before satellite delivery. We successfully sent commands and received data over the RF link with the CubeSat at an off-site location running off of its battery and solar panels. The ground station continues to be used and tested with an identical, spare version of the satellite built specifically for testing and calibration purposes.

2.7. Passive Magnetic Attitude Control System

CSSWE uses a passive magnetic attitude control system (MACS) that aligns the CubeSat to the Earth's local magnetic field line at all points in the orbit. The system is composed of two primary elements. The first is a bar magnet, which has a magnetic moment of 0.81 Am^2. Its dipole axis is parallel with the long axis of the spacecraft, and it provides a restoring torque toward the local magnetic field of the Earth. The second is an array of soft-magnetic hysteresis rods mounted perpendicular to the bar magnet, which are magnetized by the local earth field. As the satellite rotates, the relative orientation between the hysteresis rods and the local earth magnetic field changes, which changes the polarity of the rods. Energy is lost to heat as the magnetic domains within

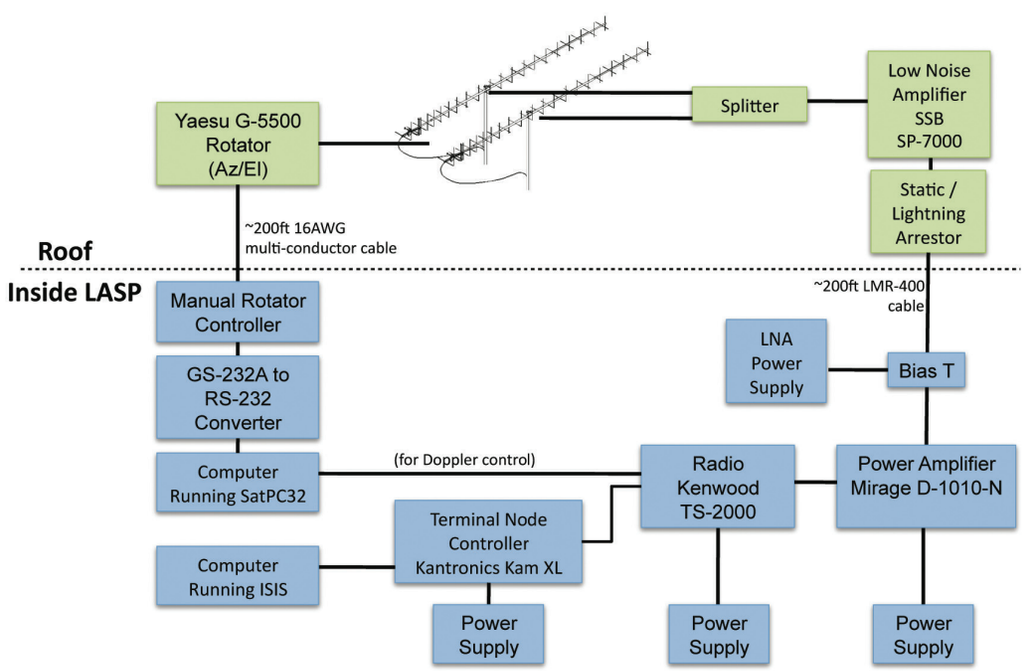

Figure 7. Ground station block diagram. Commands are packetized by the ground station software ISIS, passed through the terminal node controller and radio, where the signal is modulated about the assigned UHF frequency, 437.345 MHz, amplified ~10× by the Mirage D-1010-N power amplifier and transmitted through two Yagi antennas on the LASP roof. On the downlink, the signal is received and amplified ~24 dBm by the SSB SP-7000 low-noise amplifier and passed back through the RF chain to the ground station software. The pointing of the Yagi antennas is determined via a second computer running the tracking program SatPC32, which controls the azimuth-elevation rotator on the roof.

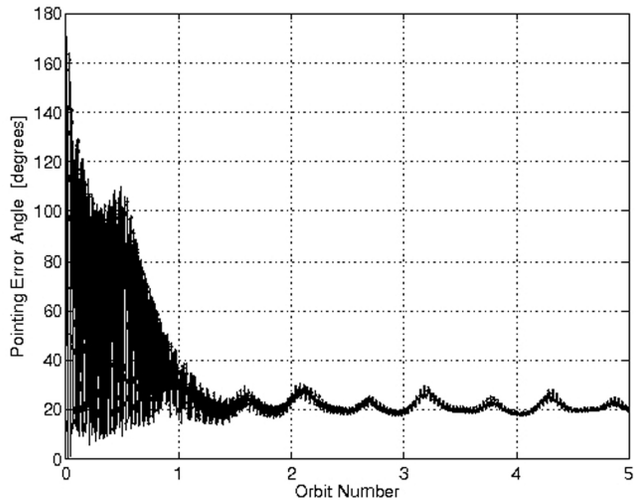

Figure 8. Expected CSSWE long-axis-pointing direction versus local magnetic field as a function of time (orbit number) after launch.

the hysteresis rods change direction. This energy loss serves to dampen the satellite rotation until the satellite bar magnet axis is roughly aligned with the local earth field direction.

The CSSWE team has developed a passive magnetic attitude control simulation to model the spacecraft attitude over time. The exact magnitude of the torque due to the hysteresis rods is of paramount importance to such a model. Thus, a Helmholtz cage test setup was built to measure the rod magnetic moment versus the axial earth field. This measurement method seeks to provide accurate inputs to the simulation. Figure 8 shows the simulated earth field to satellite bar magnet axis angle over the first five orbits, assuming an initial angular offset of 180° and an initial spin rate of 18° min^{-1} (the expected initial spin rate for our specific launch). As shown from simulations, the satellite is expected to settle to a constant offset from the local magnetic field within two orbits and to oscillations of ±10° from this offset. The expected settling time is short because the expected initial spin rate is low. A calibrated magnetometer is located on board to provide two-axis attitude knowledge during operations. Two-axis attitude knowledge (relative to the earth's magnetic field) is expected within ±3°. Photodiodes on each of the solar arrays have also been installed to provide three-axis attitude knowledge when the spacecraft is insolated.

2.8. Relativistic Electron and Proton Telescope Integrated Little Experiment

As mentioned previously, the instrument on board CSSWE will consist of a particle telescope to make differential measurements of energetic protons and electrons. Solid state detectors are often used to measure energetic particles in space, although challenges for such instrument designs still remain. For example, relativistic electrons scatter erratically upon interacting with matter; therefore, the amount of energy they deposit into a specified volume of material, and thus the initial energy of the electron, must be determined statistically. Protons, on the other hand, deposit energy according to the Bethe-Bloch formula as they travel. At high-energy (several tens of MeV), they have the ability to penetrate through the instrument shielding and impact the detectors from all directions. These characteristics of both species of particles must be accounted for in order to design a reliable energetic particle instrument.

2.8.1. Telescope design. The REPTile detector stack consists of four solid state silicon detectors similar to those used for the RBSP/Relativistic Electron and Proton Telescope (REPT) instruments, which have been delivered for a launch that occurred on 30 August 2012 (D. N. Baker et al., The Relativistic Electron-Proton Telescope (REPT) instrument on board the Radiation Belt Storm Probes (RBSP) spacecraft: Characterization of Earth's radiation belt high-energy particle populations, submitted to *Space Science Review*, 2012, hereinafter referred to as Baker et al., submitted manuscript, 2012). To minimize contamination from particles outside the instrument field-of-view, these detectors are housed in a tungsten (atomic number $Z = 74$) chamber, which is encased in aluminum ($Z = 13$) shielding. The outer aluminum shield serves to absorb most electrons and lower-energy protons while significantly reducing the energy of incident higher-energy protons, which can produce showers of contaminating secondary particles in high-Z materials. The dense, high-Z tungsten shield significantly increases the energy threshold at which protons can fully penetrate into the detector stack, effectively reducing the background flux. This layered shielding effectively blocks electrons with energy less than ~15 MeV and protons with energy less than ~75 MeV. Additional tungsten shielding at the rear of the detector stack prevents protons with energy less than ~90 MeV from penetrating the end-cap shielding, where the geometric factor is large (see Figure 9).

A shielded, baffled collimator defines the instrument's 52° field-of-view and its 0.526 sr cm^2 geometric factor. Particles that enter the detector stack through the collimator are filtered by a thin beryllium ($Z = 4$) foil, which acts as a high-energy pass filter, absorbing electrons with energy less than ~ 400 keV and protons with energy less than ~8 MeV. These energies correspond approximately to the lowest detectable energy of the instrument. Knife-edged collimator baffles have been designed such that no particle can enter the

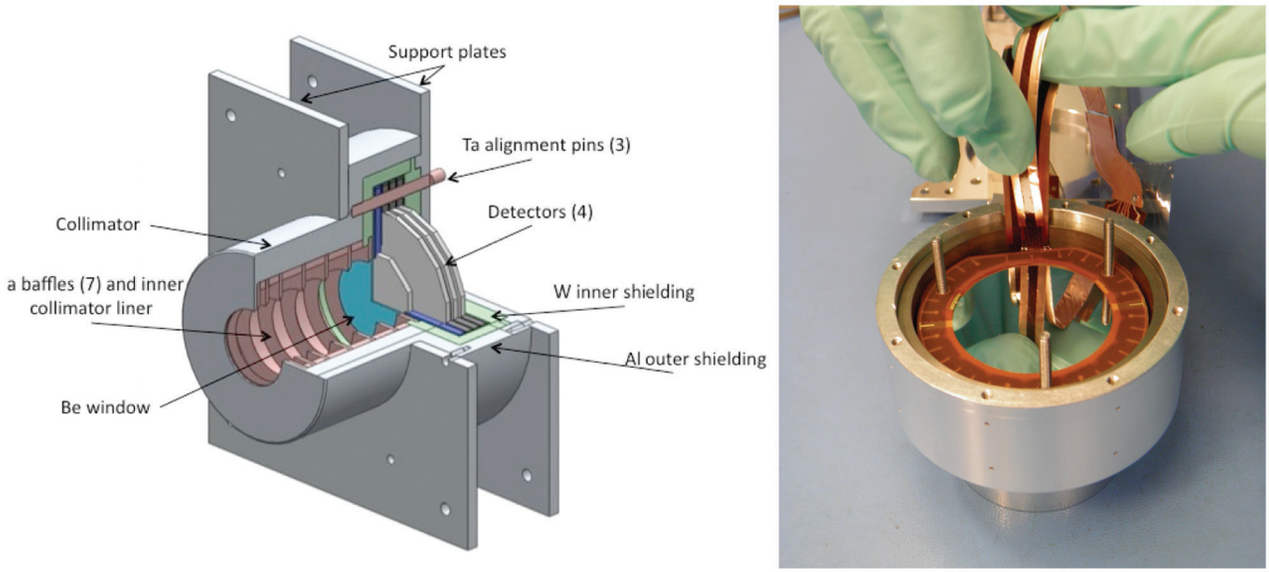

Figure 9. (left) Cross-sectional view of the instrument geometry. (right) Flight instrument during integration. The collimator is facing down in the image, and the back plate not yet attached, so the detector stack is visible.

detector stack without at least two reflections from an interior surface of the tantalum collimator. Tantalum (Z = 73) was chosen for the inner collimator lining and baffles as it provides a balance between stopping power and secondary particle characteristics.

2.8.2. Electronics design. The REPTile electronics perform three primary functions: (1) to recognize particles that hit the detectors, (2) to determine the particle species and incident energy, and (3) to convert the analog pulses to a digital signal to relay to C&DH. The system-level signal chain block diagram for one detector can be seen in Figure 10. The charge deposited into the detector by an incident particle (step 1) is swept from the silicon with a ~350 V bias voltage to the charge-sensitive amplifier (CSA, step 2). Since the CSA must be capable of amplifying small signals from the detector, it is very sensitive to noise, and great care is taken to filter the signal and remove offsets from variations in temperature.

The second stage of amplification occurs at the pulse-shaping amplifier (step 3) and is used to further distinguish the voltage levels corresponding to electrons and protons. The analog pulse is converted to digital at a three-level discriminator chain (step 4), where the discriminator thresholds are set to the equivalent of 0.25, 1.5, and 4.5 MeV deposited in the detector. The discriminator chain is used to distinguish the species of particle, where particles depositing 0.25 MeV < $E \leq$ 1.5 MeV are considered electrons, and particles depositing E > 4.5 MeV are binned as protons. The complex programmable logic device (step 5) simultaneously

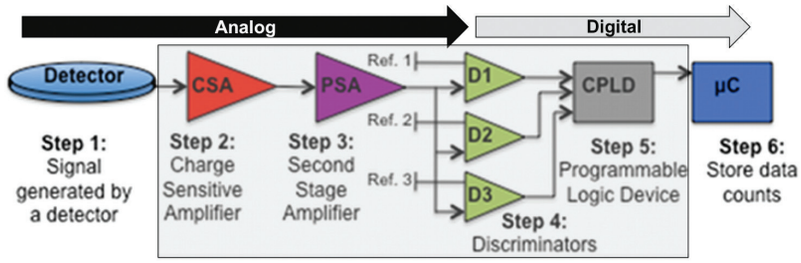

Figure 10. REPTile electronics block diagram for a single detector signal chain. The gray box corresponds to components on the REPTile electronics board.

Table 1. Coincidence Logic for Particle Binning[a]

		Detector			
Species	Energy (MeV)	1	2	3	4
Electron	0.5–1.5	100	000	000	000
Electron	1.5–2.2	X00	100	000	000
Electron	2.2–2.9	X00	100	100	000
Electron	>2.9	X00	100	100	100
Proton	8.5–18.5	111	000	000	000
Proton	18.5–25	1XX	111	000	000
Proton	25–30.5	1XX	111	111	000
Proton	30.5–40	1XX	111	111	111

[a]Each trio of bits represents the output of the three discriminators for that detector. A 1 signifies the threshold has been surpassed, and a 0 signifies the threshold has not been achieved. An X signifies that either a 1 or a 0 satisfies the logic. The bits correspond to, from left to right, the 0.25, 1.5, and 4.5 MeV references.

interprets the signals from all four detectors, and if the comparator outputs satisfy the binning logic outlined in Table 1, increments the appropriate counter. Every 6 s, the totals of each counter are sent to the C&DH (step 6).

2.8.3. Instrument characterization. The performance of the REPTile instrument is characterized using the Geant4 software package, which was designed by nuclear physicists at the European Organization for Nuclear Research. Geant4 was created to simulate particle beam tests and describe the passage of particles through matter, and it has been used to determine the performance of the Large Hadron Collider and the Tevatron collider at Fermilab.

Geant4 creates a virtual environment in which the instrument is assembled and bombarded with particles. The simulation quantifies the energy deposited into each detector for each incident particle. Figure 11 is a visualization of raw Geant4 data consisting of a wireframe instrument geometry and particle tracks through the environment. The electron tracks are red, protons are blue, and bremsstrahlung radiations are green. The left panel depicts a 2 MeV electron beam fired down the collimator from the left that, upon impacting the beryllium foil, begins to diverge into a scatter cone. The electrons then interact with the four silicon detectors, sometimes producing bremsstrahlung radiation. Some backscattering occurs: one electron reverses direction and embeds itself in the collimator wall. The right panel portrays a 20 MeV proton beam fired down the collimator. Proton scattering is minimal, and after passing through the first detector, the protons embed themselves in the second. The protons create low-energy electron showers when interacting with matter, so the proton tracks appear red when inside the silicon detectors.

Simulations are conducted for all incident angles and particle energies. The efficiency response of each detector is determined as a function of incident energy, as seen in Figure 12. For each energy increment, 10,000 particles are fired into the detector stack. The percent of particles that impact a detector are plotted in black, and the percent of particles that get logically binned in the corresponding energy channel (based on the logic outlined in Table 1) are plotted in red. The protons are relatively well behaved, and the channel thresholds are clearly defined. The electron channels, however, are more difficult to specify due to the random interactions inside the instrument. The energy channels are chosen

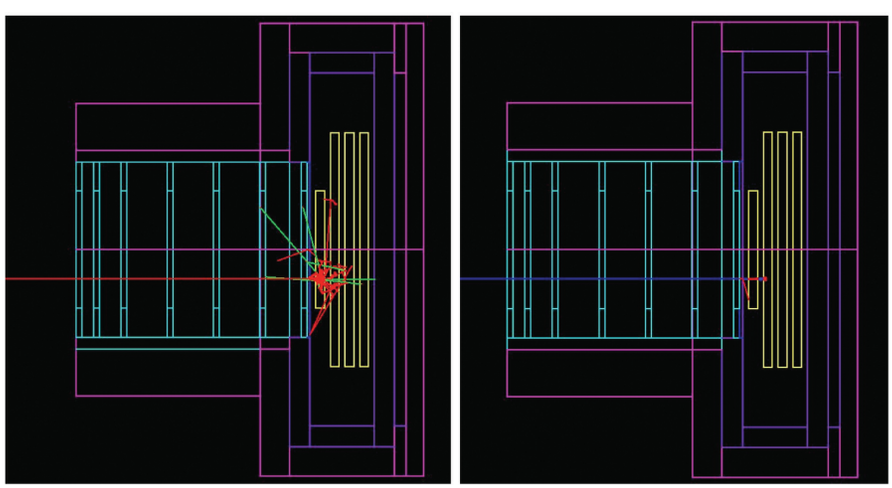

Figure 11. (left) A 2 MeV electron beam fired down the collimator of the REPTile instrument. Electrons (red) interact with the detectors and shielding, producing high-energy photons (green). (right) A 20 MeV proton beam fired down the collimator. Protons (blue) interact with the first detector and are embedded in the second detector.

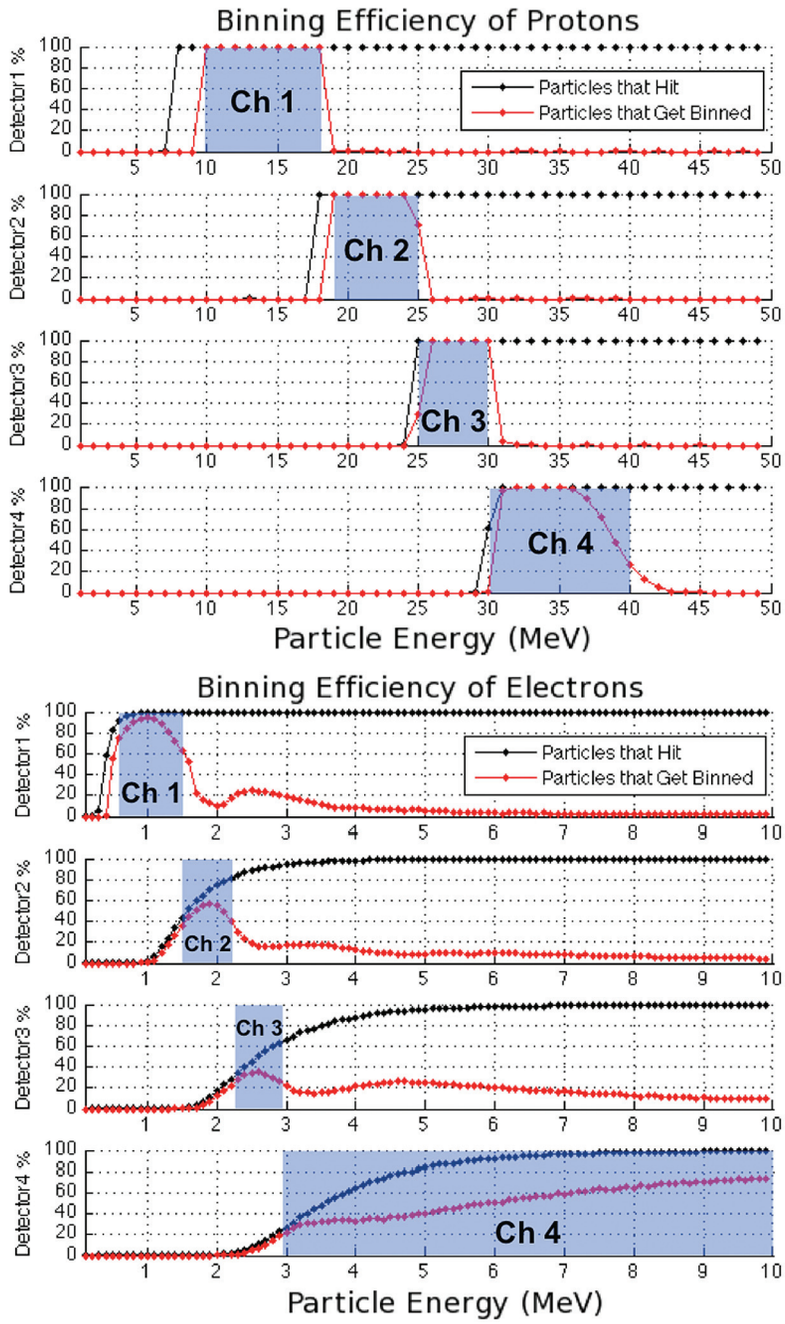

Figure 12. Response function of all four detectors for (left) protons and (right) electrons.

to maximize the response of each detector corresponding to the most efficient binning profile, which is shown in Figure 13. The energy deposited into each of the four detectors is plotted as a function of incident energy for electrons. The horizontal dashed lines correspond to discriminator thresholds of 0.25 and 1.5 MeV, between which the particle is classified as an electron. The vertical solid lines correspond to the electron energy range of the corresponding detector. The detectors discard 2.7%, 44.6%, 40.1%, and 30.4%, respectively, of the electrons in their appropriate energy range. The discriminator thresholds can be changed in-flight through uplink commands. Thus, if the ambient electron flux

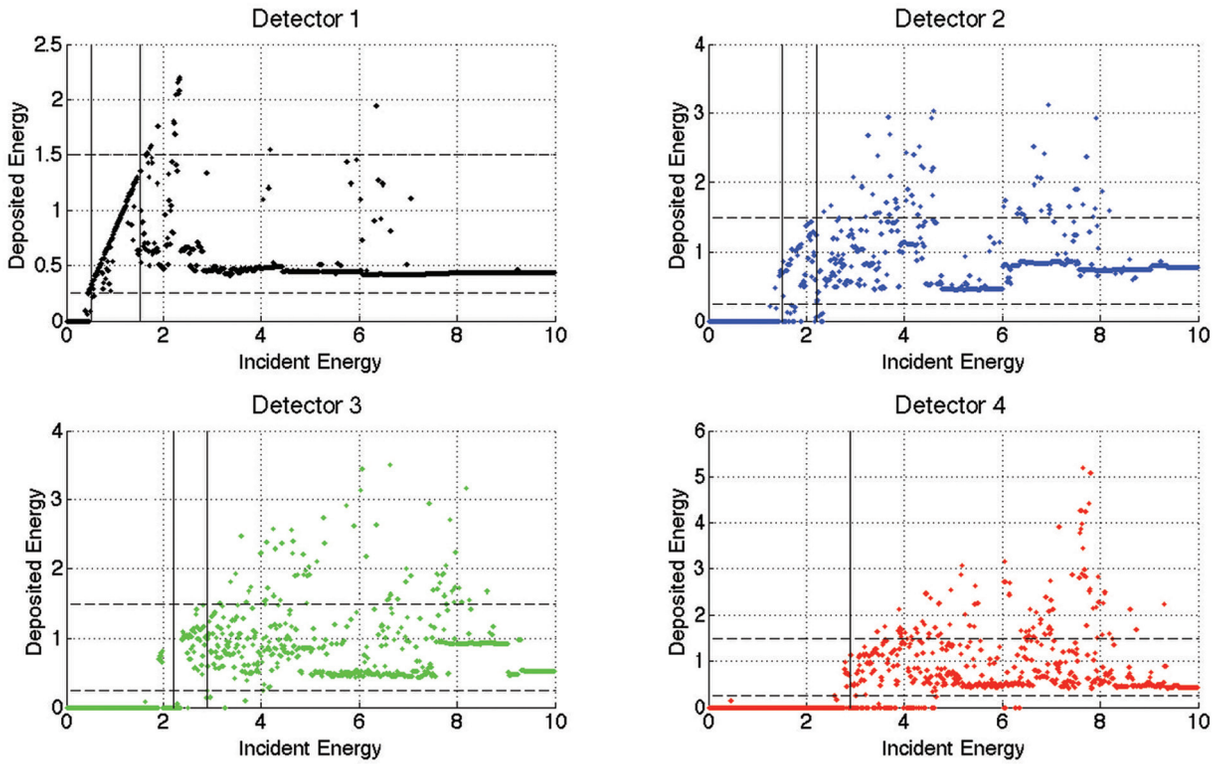

Figure 13. Energy deposited into all four detectors as a function of incident energy from a simulation of 20,000 electrons in Geant4. The horizontal dashed lines correspond to the 250 keV and 1.5 MeV discriminator thresholds, in between which the particle is binned as an electron. The vertical solid lines correspond to the energy range of the corresponding detector.

is very high, the upper-energy threshold can be lowered. With a lower threshold, fewer electrons are measured, but the measurements are cleaner, making the conversion from count rate to flux more reliable.

Additionally, the proficiency of the instrument's shields is determined by firing particle beams into the shielding. The particles that interact with the shielding or collimator before entering the detector stack are considered instrument noise. The field-of-view flux is contaminated largely by particles penetrating the rear shielding, motivating the additional tungsten shielding there. The analysis is performed assuming energy spectra during the most active times for each species: the electron spectrum from the AE8 solar max model (http://modelweb.gsfc.nasa.gov/models/trap.html) is modeled as $I(E) = 3.003 \times 10^5 E^{-2.3028}$, and the proton spectrum from data presented in the work of *Mewaldt et al.* [2005], from one of the largest SEP events in the last 50 years, is modeled as $I(0.1\ \text{MeV} \leq E \leq 26\ \text{MeV}) = 5.20 \times 10^4 E^{-1.1682}$ and $I(E > 26\ \text{MeV}) = 9.65 \times 10^8 E^{-4.2261}$. Despite the extreme spectrum assumptions, REPTile still meets the required S/N ratio of ≥ 2 for all channels. The detailed S/N ratio for each channel is outlined in Table 2.

The permanent magnet used for CSSWE's attitude control will alter incident particles' trajectories. Test-particle simulations were performed using the relativistic Lorentz force to simulate the possible effects on the REPTile measurements. In these simulations, a constant value for the Earth's magnetic field at LEO is used as a background field and a dipole magnetic field, centered directly behind the instrument (significantly closer than the actual magnet location), is included. The magnet is far enough from REPTile to assume a dipolar field, and the strength of the magnet's dipole is calculated using its magnetic moment. Test particles of both protons and electrons are fired down the bore sight of REPTile from a distance of 1 m. This initial position is small compared to the particles' gyroradii but large with respect to the ADCS magnetic field. The initial velocities for electrons corresponding to

Table 2. S/N Ratio for Electrons and Protons on All Four Detectors, Calculated for Extreme Energetic Particle Conditions

	Detector 1	Detector 2	Detector 3	Detector 4
Electron S/N	88.3	18.7	13.0	10.4
Proton S/N	13.6	7.0	5.3	2.0

10 eV to 5 MeV and for protons 1 keV to 50 MeV are used. Based on the results of this analysis, the Attitude Control Systems (ADCS) magnet alters the trajectories of only lower-energy electrons ($E < \sim 10$ keV) near REPTile. The effect of the ADCS magnet on relativistic electrons and energetic protons that enter through REPTile's field-of-view is negligible; thus, the instrument's performance is unaffected by its presence.

2.8.4. Instrument testing. Without access to particle accelerators due to budgetary constraints, the fully assembled spacecraft was tested with a strontium-90 radiation source fastened to the outside of the REPTile collimator. Strontium-90 has a half-life of 28 years and decays into yttrium-90, emitting an electron with maximum energy of 0.546 MeV. Yttrium-90 has a half-life of 2.7 days and decays into zirconium-90, emitting an electron with maximum energy of 2.28 MeV. Both isotopes emit electrons in a continuous kinetic energy spectrum from zero to the maximum. An independent empirical measurement of the strontium-90 spectrum was made and fit to a power law. Using the fit, the theoretical count rate for each of REPTile's differential energy channels was calculated. Data collected from the fully integrated strontium-90 test agreed with the theoretical count rate within expectation, confirming functionality of the instrument and despite the design challenges presented by an energetic particle telescope for a CubeSat platform.

3. MISSION OPERATION, DATA ANALYSIS, INTERPRETATION, AND MODELING

3.1. CSSWE Operational Scenario

The expected orbit is 480 km × 790 km, with an inclination of 65°. Once deployed from the launch vehicle, the spacecraft will power on, start charging batteries and begin to align itself with the Earth's magnetic field using a passive MACS, described earlier. Simulations have shown that, based on the orbit average power, the spacecraft will be power positive. The 8.4 W h batteries should charge to full capacity within 24 h on orbit. The system starts up in safe mode, transmitting a beacon every 18 s to aid in establishing contact with the ground station. The mission design allows 1 month for spacecraft contact and commissioning before the 3 month science mission, as illustrated in Figure 14. Student operators will establish contact and operate the spacecraft under the guidance of the experienced LASP mission operators using the ground station located at LASP.

The spacecraft passes over the Boulder ground station an average of 4.7 times each day with an average link time of 4.5 min available to download data on each pass. Accounting for an assumed 20% dropped packets, CSSWE can downlink 40% of the science data, and all housekeeping data generated in 1 day using only two (of the anticipated 4.7) 4.5 min passes. Because only high-latitude data is of interest for the mission, the science data may be selectively downlinked by accounting for satellite position when the data was recorded. However, because the entirety of the science mission can be stored on board the satellite SD card, data for any time can be requested during any pass. Thus, data from an interesting solar event that would be measured by REPTile even at low latitudes may be downlinked after the event has occurred.

3.2. Data Analysis and Interpretation

CSSWE will store science data on board until contact with the LASP ground station is made. Upon requests for specific time intervals, the satellite will return science data as time-stamped attitude information, spacecraft mode, detector

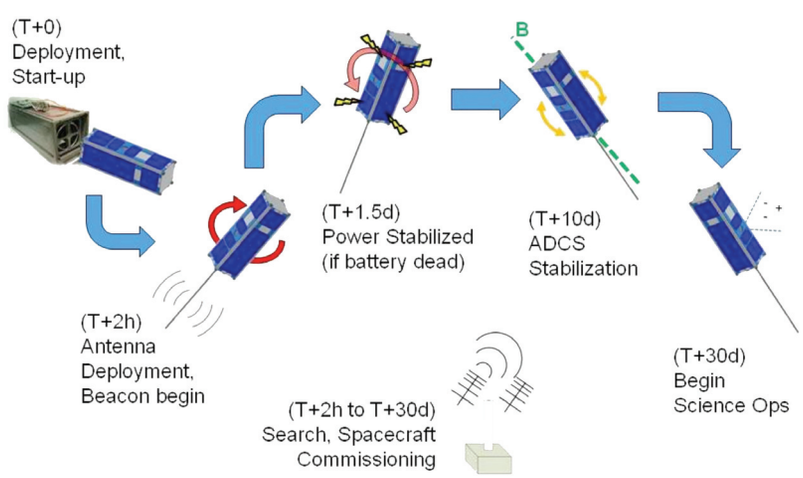

Figure 14. The early mission operations of the satellite are shown.

status, and binned electron and proton counts at 6 s cadence. The raw science packets will be received and parsed at the ground station at LASP using ISIS command and control software and saved as level 0 text files of raw count rates, raw magnetometer, and photodiode values (used later for attitude determination), spacecraft mode, and detector status. Corrections are then applied to these level 0 raw count rates to create level 1 data.

The conversion of level 0 count rate data into level 1 count rates will correct for background and dead time effects. Corrections will account for the charge collection time in the detector, which is 250~300 ns for 1.5 mm silicon. By assuming a Poisson distribution with 6 s cadence, a statistical correction can be made for the charge collection time. Additional corrections will be applied to account for electronic pileup, where the pileup time scale is ~8 μs. Pileup is dependent on the performance of specific electronic components.

The CSA, shown in Figure 10, has an inherent temperature-dependent exponential offset. The onboard electronics remove the offset to first order, but for periods where the first-order approximation breaks down, warning flags of various levels will be included with the data. Additionally, the accuracy of the CSA decreases during periods of high fluxes. Onboard corrections allow for some science to be recovered during these periods, but warning flags will also be included to indicate increasingly unreliable data. Additional warnings will be issued for other inconsistencies, such as improperly biased detectors or changes in discriminator threshold voltages. A copy of the flight hardware has been fabricated and will be used for additional calibration, as this flight spare behaves identically to the delivered CubeSat.

Level 2 data take the adjusted count rate (level 1) data and converts them into fluxes at designated energy ranges. We use bowtie analysis to derive an incident energy spectrum $f(E)$ for both electrons and protons based on a best fit to the data using the following equation:

$$C_i = \int \gamma f(E) \alpha_i(E) \mathrm{d}E, \tag{1}$$

where C_i is the count rate for channel i, γ is the instrument geometric factor, f is the environmental particle flux, and α_i is the response function of detector i, as calculated from Geant4 simulations. The flux on each detector is then calculated based on the derived best fit energy spectrum. The differential fluxes will be provided as level 2 data, as well as the energy spectrum used, and a measure of the error in the spectral fit to the data.

Finally, level 3 data are the differential flux measurements converted into directional differential flux. This is done using the onboard magnetometer data (and photosensors mounted on four sides of the solar array if the satellite is insolated) to determine the direction of the local background magnetic field relative to the alignment of the spacecraft. We then derive the look direction of the instrument to resolve the PA range of the measured particles. Using a magnetic field model, such as the *Tsyganenko* [2002] model, we map the magnetic field lines to the equator and determine the L value (equatorial radial distance in the Earth radii from the center of the Earth) and the equatorial PA of the particles (Table 3).

Table 3. Data Level Description

Data Level	Description
Level 0	Raw 6 s electron and proton count rates
Level 1	Adjusted count rates, accuracy flags
Level 2	Differential flux per detector and species, estimated energy spectra, and error
Level 3	Directional differential flux, pitch angle, and L shell

3.3. Modeling

Owing to the nondipolar nature of the Earth's magnetic field and CSSWE's orbit and orientation, the electrons measured by CSSWE can be categorized as a mixture of trapped, quasitrapped (in the drift loss cone (DLC)), and precipitating (in the bounce loss cone (BLC)) populations, depending on where (i.e., longitude and latitude in the Northern and Southern Hemispheres) the measurements are made [*Selesnick*, 2006; *Tu et al.*, 2010]. The BLC is defined as the range of equatorial PAs where an electron's mirror point reaches at or below an altitude of 100 km in either hemisphere (with electrons lost within one bounce period), and the DLC is defined as the range of equatorial PAs between the highest BLC angle at the South Atlantic Anomaly (SAA) region and the local BLC angle (electrons lost within one drift period). Figure 15a illustrates the identification of these three different populations based on a comparison of the equatorial PA for electrons mirroring at CSSWE's altitude (~600 km) at $L = 4$. The equatorial BLC angles across longitude (the upper boundary of the red area) are in the range of 5.2° to 6.8° in equatorial PA, with the highest near SAA (near 0° and 360°) and the lowest near 105° geomagnetic longitude. The equatorial PA of a data point is estimated by assuming it is locally mirroring at the satellite location, which is an approximation considering the wide field-of-view of the detector. Under this assumption, some of the so-called "trapped" electrons may actually be quasitrapped (if the actual local PA < 90°), or some "quasitrapped" electrons may actually be untrapped, but the "untrapped" electrons will be truly untrapped. Thus, using this approximation, we calculate the lower bound on

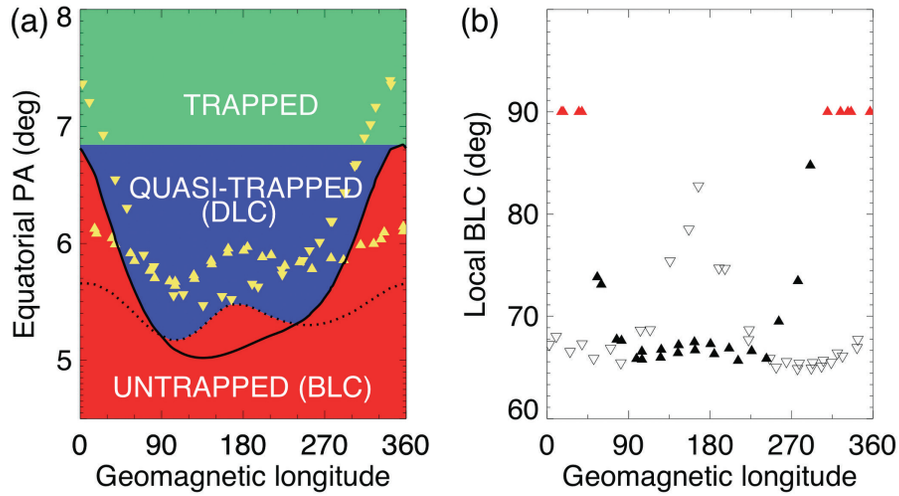

Figure 15. (a) Schematic illustration of three populations of energetic electrons that can be measured by CSSWE (600 km altitude): trapped, quasitrapped, and untrapped, depending on their equatorial pitch angle (PA) ranges (shown here at $L = 4$) and where the measurement was made (i.e., longitude and latitude in the Northern and Southern Hemisphere). When an electron reaches below 100 km altitude, it is assumed to be lost. The upward triangles represent measurements taken in the Northern Hemisphere and the downward ones in the Southern Hemisphere. The solid (dotted) curve represents the bounce loss cone (BLC) angle at $L = 4$ in the Southern (Northern) Hemisphere, so the final BLC at each longitude is the maximum of these two, with the range of equatorial PA inside the BLC filled by red color. (b) Local BLC angles at the measurement locations (upward solid and downward empty triangles) in Figure 15a, with the untrapped electron measurements in red (untrapped: these electrons, even mirroring at the measurement location, will be lost by reaching at 100 km at the other hemisphere).

precipitation loss, equal to or less than the actual flux of precipitating electrons.

This can be seen from Figure 15b, where the calculated local BLC angles, corresponding to the triangles in Figure 15a, are displayed, more of which are less than 90°. The corresponding untrapped electrons (red triangles) are measured at the location with local BLC at 90° (meaning they will be lost by reaching at or below 100 km in the other hemisphere even if they mirror at the measurement location).

Since the observed electron flux variation is a complicated balance between loss and energization for any quantitative study, physical modeling is needed. REPTile provides a 6 s integration measurement of the particle distributions, which contain a mixture of the three different populations, in varying proportions depending on longitude and hemisphere. To determine the precipitation loss from these data, modeling efforts are required. We have analyzed and modeled 6 s integration measurements of MeV electrons from SAMPEX, which was in a similar orbit and is expected to reenter the atmosphere soon [*Baker et al.*, 2012]. For example, Figure 16 shows energetic electron measurements by P1 and ELO channels on SAMPEX, represented by the filled triangles as a function of longitude when SAMPEX crossed $L = 4.5$ during a geomagnetic storm in 8–13 March 2008. The empty triangles are simulation results, to be discussed later. Figure 16a shows a typical quiet time prior to a magnetic storm; Figure 16b immediately follows Figure 16a in time and includes the magnetic storm main phase, Figure 16c is during the storm early recovery phase, and Figure 16d commences the late recovery phase. The general pattern and variation of the data are the stably trapped population near 0° and 360° longitude in the south (green triangles pointing downward) has the highest count rates before the storm, decreases significantly during the storm main phase and stays low in the early recovery phase, and then returns to the prestorm level during the late recovery phase; the quasi-trapped population in the DLC from ~45° to 315° longitude (blue points) has intermediate data rates and increases eastward during the prestorm and late recovery phases because of the azimuthal drift, during the storm main phase it is relatively flatly distributed over the longitude; the untrapped population in the BLC near 0° and 360° in the north (red upward triangles) generally has the lowest count rates. Based on only the measurements, little physical information can be extracted. We have developed a drift-diffusion model at LASP that includes azimuthal drift and PA diffusion to simulate the low-altitude electron distribution observed at LEO to quantify the electron precipitation loss into the

atmosphere [*Tu et al.*, 2010]. The model is governed by the equation:

$$\frac{\partial f}{\partial t} + \omega_d \frac{\partial f}{\partial \phi} = \frac{\omega_b}{x}\frac{\partial}{\partial x}\left(\frac{x}{\omega_b} D_{xx} \frac{\partial f}{\partial x}\right) + S, \qquad (2)$$

where $f(x, \phi, t)$ is the bounce-averaged electron distribution function at a given L shell and kinetic energy E, as a function of $x = \cos \alpha_0$ (where α_0 is the equatorial PA), drift phase ϕ, and time t; ω_d is the bounce-averaged drift frequency; ω_b is the bounce frequency; D_{xx} is the bounce-averaged PA diffusion coefficient, in the form

$$D_{xx} = D_{\mathrm{dawn/dusk}}\, \tilde{E}^{-\alpha} \frac{1}{10^{-4} + x^{30}}, \qquad (3)$$

where $\tilde{E} = E/(1\ \mathrm{MeV})$; and S is the source rate, defined as

$$S = S_0\, \tilde{E}^{-\nu} \bar{g}_1(x)/p^2, \qquad (4)$$

where $\bar{g}_1$ is the lowest-order eigenfunction of the combined drift-diffusion operator (the terms in equation (1) involving $\partial/\partial\phi$ and $\partial/\partial x$), and p is the electron momentum for a given E. Free parameters include D_{dawn}, D_{dusk}, α, ν, and S_0.

By adjusting model-free parameters, we can fit the longitude dependence of the electron count rates in the model to the data. The best fit simulation results, shown as empty triangles in Figure 16, determine the PA diffusion coefficients of electrons at different energies for different intervals. Then, the electron lifetime at a specific energy can be estimated as: $\tau = 1/(100\bar{D})$, where $\bar{D}$ is the longitude-averaged model diffusion coefficient defined as $\bar{D} = (D_{\mathrm{dawn}} + D_{\mathrm{dusk}})\tilde{E}^{-\mu}/2$.

4. SUMMARY

Here we have provided a detailed description of the upcoming Colorado Student Space Weather Experiment, an NSF-funded CubeSat mission launched on 13 September 2012 (our ground station was able to find, track, and receive beacon/housekeeping packets during the first pass around 04:00 LT next day, all appear nominal at this point). The CSSWE system architecture has been designed to maintain simplicity while meeting all of the well-defined and justified system and subsystem requirements. A "keep-it-simple" architecture mitigated risk and allowed the CSSWE team to design, manufacture, and test a fully functional satellite, which was successfully delivered on time to the launch provider with additional margin on the various system requirements defined for CubeSats. Housed within the 3 U CubeSat structure, the combined CSSWE subsystems provide the necessary platform to achieve CSSWE's primary

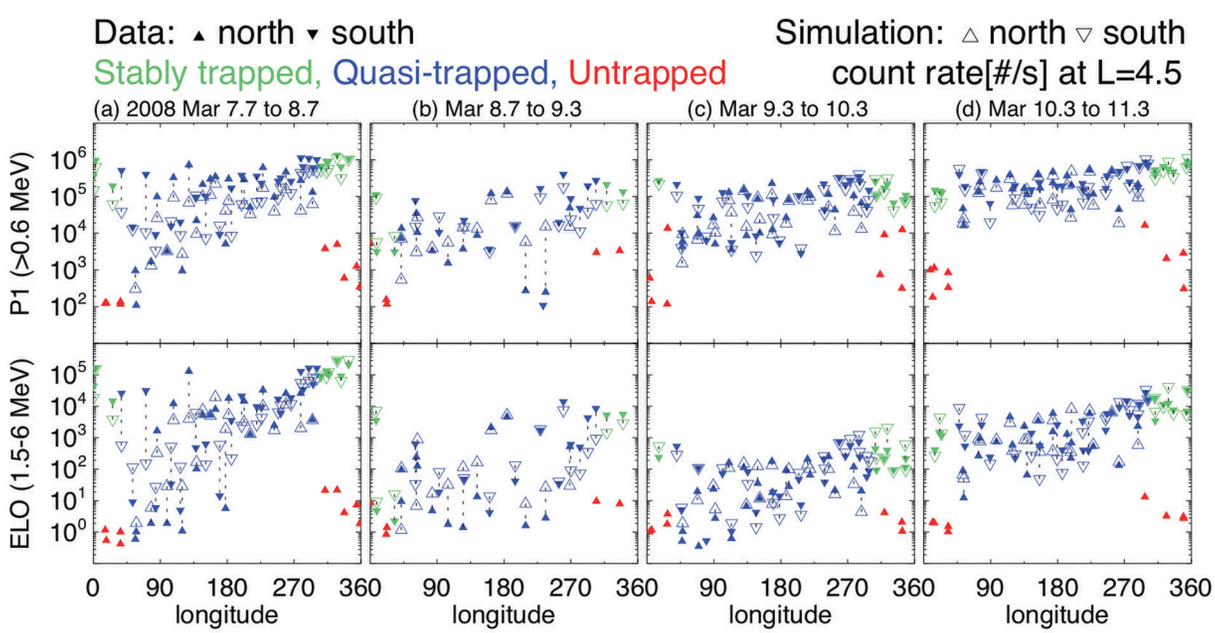

Figure 16. Electron count rate data (solid triangles) at L = 4.5 from two SAMPEX channels (P1 and ELO) versus geomagnetic longitude during (a) a quiet prestorm interval, (b) storm main phase, (c) early recovery phase, and (d) late recovery phase of the March 2008 storm. Data points are identified as trapped (green), quasitrapped (blue), and untrapped (red). Upward triangles are measured in the Northern Hemisphere and downward ones in the Southern Hemisphere. The simulation results are shown as empty triangles.

science goals to make differential flux measurement for energetic electrons and protons. Under the tutelage of Aerospace Engineering professors and LASP scientists and engineers, graduate students designed, built, and tested the internal structures, thermal, power, ground station, and attitude control subsystems, while COTS C&DH and communications subsystems and an external frame were integrated as well. Also, student designed and tested, CSSWE's primary science payload, REPTile, will observe solar energetic protons in the energy range 10–40 MeV and outer radiation belt electrons in the energy range 0.5 to >3 MeV. The necessary environmental tests and thorough end-to-end testing of each of the subsystems, and the fully integrated spacecraft with communication to the ground station, have been successful, providing confidence that CSSWE will perform as designed when on orbit.

Science data from REPTile will be processed and released using multiple levels of refinement, from raw, unprocessed count rates (level 0) to directional, differential energy fluxes with specified PA ranges and L shells (level 3). We have also discussed one application of how this data can be used to understand precipitation loss of outer radiation belt electrons based on the work of *Tu et al.* [2010]. This drift-diffusion model will use REPTile electron fluxes to quantify electron loss rates into the Earth's atmosphere. When SEPs occur, CSSWE will also be used to determine the energy spectra, intensity, and latitudinal extent of these ultraenergetic particles precipitating into the Earth's atmosphere. These are just two examples of how CSSWE science data will be used, but many more studies can be conducted, especially when the data are used in conjunction with data from other missions, such as SDO, RBSP, and/or Time History of Events and Macroscale Interactions during Substorms (THEMIS).

CubeSat missions are gaining popularity in the scientific community, and CSSWE is a prime example of their potential. Alongside the other NSF CubeSats (e.g., RAX [*Cutler et al.*, 2010] and CINEMA [*Lee et al.*, 2011]), CSSWE is proving how small, inexpensive, student-built and designed space missions are not only feasible, but fully practical for achieving valuable science objectives. CSSWE science observations will help to address unanswered questions concerning the nature and impact of solar energetic proton events at Earth. Additionally, by providing observations of pitch angle resolved relativistic electrons at LEO, CSSWE will complement NASA's RBSP mission to understand Earth's highly variable outer radiation belt. This demonstrates how, for an additional cost that is only a small fraction of the total mission cost, large, expensive science missions can benefit from one or more small spacecraft, like CubeSats, to provide additional points and types of measurements, particularly those that may be impossible for the larger mission to provide on its own.

Acknowledgments. The authors thank other CSSWE team members who are not listed here, as well as LASP scientists and engineers: D. N. Baker, T. Woods, J. Gosling, G. Tate, M. McGrath, W. Possell, V. Hoxie, S. Batise, C. Belting, K. Hubbell, J. Young, S. Worel, G. Allison, E. Wullschleger, P. Withnell, and V. George. We also thank Jamie Culter of U. of Michigan for consultation and support for the EPS and Comm system, R. Strieby, and R. Kile of Loveland Repeater Association for their help and support for the Ground Network and Comm system, and Jim White for his help and support on various aspects of the CSSWE mission. This work was supported by NSF (CubeSat program) grant AGSW 0940277.

REFERENCES

Aschwanden, M. J. (2004), *Physics of the Solar Corona: An Introduction*, Springer, Berlin.

Baker, D. N. (2001), Satellite anomalies due to space storms, in *Space Storms and Space Weather Hazards*, edited by I. A. Daglis, chap. 10, pp. 251–284, Springer, New York.

Baker, D. N. (2002), How to cope with space weather?, *Science*, *297*, 1486–1487.

Baker, D. N., P. R. Higbie, R. D. Belian, and E. W. Hones Jr. (1979), Do Jovian electrons influence the terrestrial outer radiation zone?, *Geophys. Res. Lett.*, *6*(6), 531–534.

Baker, D. N., S. G. Kanekal, T. I. Pulkkinen, and J. B. Blake (1999), Equinoctial and solstitial averages of magnetospheric relativistic electrons: A strong semiannual modulation, *Geophys. Res. Lett.*, *26*(20), 3193–3196.

Baker, D. N., J. E. Mazur, and G. M. Mason (2012), SAMPEX to reenter atmosphere: Twenty-year mission will end, *Space Weather*, *10*, S05006, doi:10.1029/2012SW000804.

Bortnik, J., and R. M. Thorne (2007), The dual role of ELF/VLF chorus waves in the acceleration and precipitation of radiation belt electrons, *J. Atmos. Sol. Terr. Phys.*, *69*, 378–386.

Cane, H. V., and D. Lario (2006), An introduction to CMEs and energetic particles, *Space Sci. Rev.*, *123*, 45–56, doi:10.1007/s11214-006-9011-3.

Cane, H. V., D. V. Reames, and T. T. von Rosenvinge (1988), The role of interplanetary shocks in the longitude distribution of solar energetic particles, *J. Geophys. Res.*, *93*(A9), 9555–9567.

Carrington, R. C. (1860), Description of a singular appearance seen on the Sun on September 1, 1859, *Mon. Not. R. Astron. Soc.*, *20*, 13–15.

Chen, Y., G. D. Reeves, and R. H. W. Friedel (2007), The energization of relativistic electrons in the outer Van Allen radiation belt, *Nat. Phys.*, *3*, 614–617, doi:10.1038/nphys655.

Cutler, J., M. Bennett, A. Klesh, H. Bahcivan, and R. Doe (2010), The Radio Aurora Explorer – A bistatic radar mission to measure space weather phenomenon, paper presented at the 24th Annual Small Satellite Conference, Logan, Utah.

Gosling, J. T. (1993), The solar flare myth, *J. Geophys. Res.*, *98*(A11), 18,937–18,949.

Horne, R. B., et al. (2005), Wave acceleration of electrons in the Van Allen radiation belts, *Nature*, *437*, 227–230, doi:10.1038/nature03939.

Kanekal, S. G., M. Al-Dayeh, M. Desai, H. A. Elliott, and B. Klecker (2008) Relating solar energetic proton populations observed within the terrestrial magnetosphere to coronal mass ejections, magnetic flux ropes observations at 1 AU, *Eos Trans. AGU*, *89*(53), Fall Meet. Suppl., Abstract SH23B-1643.

Lee, Y., et al. (2011), Development of CubeSat for space science mission: CINEMA, paper presented at the 62nd International Astronautical Congress, Capetown, South Africa.

Leske, R. A., R. A. Mewaldt, E. C. Stone, and T. T. von Rosenvinge (2001), Observations of geomagnetic cutoff variations during solar energetic particle events and implications for the radiation environment at the Space Station, *J. Geophys. Res.*, *106*(A12), 30,011–30,022.

Li, X., D. N. Baker, M. Teremin, T. E. Cayton, G. D. Reeves, R. S. Selesnick, J. B. Blake, G. Lu, S. G. Kanekal, and H. J. Singer (1999), Rapid enhancements of relativistic electrons deep in the magnetosphere during the May 15, 1997, magnetic storm, *J. Geophys. Res.*, *104*(A3), 4467–4476, doi:10.1029/1998JA900092.

Li, X., D. N. Baker, S. G. Kanekal, M. Looper, and M. Temerin (2001), Long term measurements of radiation belts by SAMPEX and their variations, *Geophys. Res. Lett.*, *28*(20), 3827–3830, doi:10.1029/2001GL013586.

Li, X., M. Temerin, D. N. Baker, and G. D. Reeves (2011), Behavior of MeV electrons at geosynchronous orbit during last two solar cycles, *J. Geophys. Res.*, *116*, A11207, doi:10.1029/2011JA016934.

Li, W., Y. Y. Shprits, and R. M. Thorne (2007), Dynamic evolution of energetic outer zone electrons due to wave-particle interactions during storms, *J. Geophys. Res.*, *112*, A10220, doi:10.1029/2007JA012368.

Mewaldt, R. A., C. M. S. Cohen, A. W. Labrador, R. A. Leske, G. M. Mason, M. I. Desai, M. D. Looper, J. E. Mazur, R. S. Selesnick, and D. K. Haggerty (2005), Proton, helium, and electron spectra during the large solar particle events of October–November 2003, *J. Geophys. Res.*, *110*, A09S18, doi:10.1029/2005JA011038.

Paulikas, G. A., and J. B. Blake (1979), Effects of the solar wind on magnetospheric dynamics: Energetic electrons at the synchronous orbit, in *Quantitative Modeling of Magnetospheric Processes*, *Geophys. Monogr. Ser.*, vol. 21, edited by W. P. Olson, pp. 180–202, AGU, Washington, D. C., doi:10.1029/GM021p0180.

Priest, E. R. (1981), *Solar Flare Magnetohydrodynamics*, Gordon and Breach, New York.

Reames, D. V. (1997), Energetic particles and the structure of coronal mass ejections, in *Coronal Mass Ejections*, *Geophys. Monogr. Ser.*, vol. 99, edited by N. Crooker, J. A. Joselyn and J. Feynman, pp. 217–226, AGU, Washington, D. C., doi:10.1029/GM099p0217.

Sabine, E. (1852), On periodical laws discoverable in the mean effects of the larger magnetic disturbances, No. II, *Philos. Trans. R. Soc. London*, *142*, 103–124.

Selesnick, R. S. (2006), Source and loss rates of radiation belt relativistic electrons during magnetic storms, *J. Geophys. Res.*, *111*(A4), A04210, doi:10.1029/2005JA011473.

Shprits, Y. Y., N. P. Meredith, and R. M. Thorne (2007), Parameterization of radiation belt electron loss timescales due to interactions with chorus waves, *Geophys. Res. Lett.*, *34*, L11110, doi:10.1029/2006GL029050.

Smith, Z., W. Murtagh, and C. Smithtro (2004), Relationship between solar wind low-energy energetic ion enhancements and large geomagnetic storms, *J. Geophys. Res.*, *109*, A01110, doi:10.1029/2003JA010044.

Tsyganenko, N. A. (2002), A model of the near magnetosphere with a dawn-dusk asymmetry 1. Mathematical structure, *J. Geophys. Res.*, *107*(A8), 1179, doi:10.1029/2001JA000219.

Tu, W., X. Li, Y. Chen, G. D. Reeves, and M. Temerin (2009), Storm-dependent radiation belt electron dynamics, *J. Geophys. Res.*, *114*, A02217, doi:10.1029/2008JA013480.

Tu, W., R. Selesnick, X. Li, and M. Looper (2010), Quantification of the precipitation loss of radiation belt electrons observed by SAMPEX, *J. Geophys. Res.*, *115*, A07210, doi:10.1029/2009JA014949.

Turner, D. L., X. Li, G. D. Reeves, and H. J. Singer (2010), On phase space density radial gradients of Earth's outer-belt electrons prior to sudden solar wind pressure enhancements: Results from distinctive events and a superposed epoch analysis, *J. Geophys. Res.*, *115*, A01205, doi:10.1029/2009JA014423.

Vandegriff, J., K. Wagstaff, G. Ho, and J. Plauger (2005), Forecasting space weather: Predicting interplanetary shocks using neural networks, *Adv. Space Res.*, *36*(12), 2323–2327.

Williams, D. J. (1966), A 27-day periodicity in outer zone trapped electron intensities, *J. Geophys. Res.*, *71*(7), 1815–1826.

L. Blum, C. Shearer Cooper, R. Kohnert, X. Li, Q. Schiller, and N. Sheiko, Laboratory for Atmospheric and Space Physics, University of Colorado, Boulder, CO 80303, USA. (lix@lasp.colorado.edu)

D. Gerhardt and S. Palo, Department of Aerospace Engineering Sciences, University of Colorado, Boulder, CO 80303, USA.

W. Tu, Los Alamos National Laboratory, Los Alamos, NM 8754, USA.

D. Turner, Department of Earth and Space Sciences, University of California, Los Angeles, CA 90095, USA.